


Article

Exploration Vectors and Indicators Extracted by Factor Analysis and Association Rule Algorithms at the Lintan Carlin-Type Gold Deposit, Youjiang Basin, China

Xiaolong Wang ^{1,†}, Shengtao Cao ^{2,†}, Qinping Tan ^{2,*} , Zhuojun Xie ², Yong Xia ², Lujing Zheng ³, Jianzhong Liu ^{4,5}, Kelin Zhou ², Jingdan Xiao ² and Tingxian Ren ²

- ¹ School of Earth Science and Resources, Chang'an University, Xi'an 710054, China; xlwang198307@163.com
² State Key Laboratory of Ore Deposit Geochemistry, Institute of Geochemistry, Chinese Academy of Sciences, Guiyang 550081, China; caoshengtao@mail.gyig.ac.cn (S.C.); xiezhuojun@mail.gyig.ac.cn (Z.X.); xiayong@vip.gyig.ac.cn (Y.X.); chow2052@126.com (K.Z.); xiaojingdan@mail.gyig.ac.cn (J.X.); rentingxian@mail.gyig.ac.cn (T.R.)
³ Guizhou Jinfeng Mining Limited, Guiyang 550025, China; lujing_zheng@163.com
⁴ Engineering Technology Innovation Center of Mineral Resources Explorations in Bedrock Zones, Ministry of Natural Resources, Guiyang 550081, China; liujianzhong868@sina.com
⁵ Bureau of Geology and Mineral Exploration and Development, Guiyang 550018, China
* Correspondence: tanqinping@vip.gyig.ac.cn
† Xiaolong Wang and Shengtao Cao contributed equally to this work.

Abstract: The Youjiang Basin in China is the world's second-largest concentrated area of Carlin-type Au deposits after Nevada, USA, boasting cumulative Au reserves nearing 1000 t. This study examined the recently unearthed Lintan Carlin-type Au deposit within the Youjiang Basin. Factor analysis and association rule algorithms were used to identify exploration vectors and indicators essential for navigating this promising geological territory. In the Lintan mining area, the geological strata encompass the Triassic Bianyang, Niluo, and Xuman formations comprised clastic rocks, followed by the deeper Permian Wujiaping Formation with massive carbonate rocks. The orebodies are restricted to the F₁₄ inverse fault, cutting through the Xuman Formation, with an additional F₇ fault between the Wujiaping and Xuman formations. A total of 125 rock samples from the F₁₄ fault and a representative cross-section were analyzed for 15 elements (Au, Ag, As, Bi, Cd, Co, Cu, Hg, Mo, Ni, Pb, Sb, Tl, W, and Zn). The elements were divided into four groups based on cluster and factor analysis. Group 1 (Co, Cu, Zn, Ni, Tl, W, and Bi) was mainly enriched in the Xuman, Niluo, and Bianyang formations controlled by sedimentary diagenesis. Group 2 (Au, As, Hg, and Sb) was concentrated in the F₁₄ and F₇ faults, representing Au mineralization. Group 3 (Pb, Ag, and Mo) was mostly enriched near the F₁₄ and F₇ faults, displaying a peripheral halo of Au mineralization, and was probability controlled by ore-forming hydrothermal activities. Group 4 (Cd and Mo) exhibited extreme enrichment along the periphery of the F₇ fault. This pattern indicates the presence of a substantial hydrothermal alteration zone surrounding the fault, likely influenced by ore-forming hydrothermal processes. Additionally, Pb, Ag, Cd, Mo, and W are considered essential indicators for ore formation besides Au, As, Sb, Hg, and Tl. Twelve effective association rules were derived using the association rule algorithm, which can aid in discriminating Au mineralization. The spatial distributions of the 15 elements indicated that the F₁₄ fault is the main ore-bearing fracture zone, while the F₇ fault serves as the ore-conducting structure, channeling ore-forming fluids into the F₁₄ fault. Faults between the Wujiaping and Xuman formations, along with their associated reverse faults, present potential prospecting targets both within and outside the Lintan Au deposit in the Youjiang Basin. Exploration geochemical data can be fully utilized by combining factor analysis and association rule algorithms, offering key guidance for prospecting Carlin-type gold and similar deposits.

Keywords: factor analysis; association rule algorithm; mineral exploration; Carlin-type Au deposit; Youjiang Basin



Citation: Wang, X.; Cao, S.; Tan, Q.; Xie, Z.; Xia, Y.; Zheng, L.; Liu, J.; Zhou, K.; Xiao, J.; Ren, T. Exploration Vectors and Indicators Extracted by Factor Analysis and Association Rule Algorithms at the Lintan Carlin-Type Gold Deposit, Youjiang Basin, China. *Minerals* **2024**, *14*, 492. <https://doi.org/10.3390/min14050492>

Academic Editors: Behnam Sadeghi, Bimin Zhang, Walid Salama and Zhixuan Han

Received: 26 March 2024

Revised: 27 April 2024

Accepted: 1 May 2024

Published: 7 May 2024



Copyright: © 2024 by the authors. Licensee MDPI, Basel, Switzerland. This article is an open access article distributed under the terms and conditions of the Creative Commons Attribution (CC BY) license (<https://creativecommons.org/licenses/by/4.0/>).

1. Introduction

Carlin-type gold deposit is considered to be one of the most important types of gold deposits in the world, renowned for its high Au content and economically valuable [1,2]. Youjiang Basin is the second-largest district of Carlin-type Au deposits (Figure 1) and contains more than 200 Au deposits or occurrences with approximately 1000 t of total proven Au reserves [3–7]. Superficial Au resources (<500 m) in the Youjiang Basin have been gradually exhausted by extensive exploitation, necessitating urgent new prospecting methods to explore deep or concealed orebodies. Traditionally, the drilling targets of Carlin-type Au deposits in the Youjiang Basin have been identified by delineating geochemical anomalies [8–12], relying on an understanding of the deep tectonic framework obtained from geophysical surveys [13–15]. Geochemical anomalies primarily depend on the content of ore-related elements, such as Au, As, Sb, Hg, and Tl. Surprisingly, data on other metal elements such as Ag, Bi, Co, Cu, Mo, Ni, Pb, W, and Zn are often overlooked or disregarded. Nevertheless, these neglected elements could harbor valuable yet undiscovered information relevant to Au mineralization.

The primary method of ore prospecting involves the integration of geological, geochemical, geophysical, and remote-sensing data [16,17]. These data in question are typically voluminous, diverse, heterogeneous, high-dimensional, computationally complex, and subject to high levels of uncertainty, aligning closely with the defining characteristics of big data, often referred to as the “4V” characteristics. This is particularly true for spatiotemporal big data in geoscience [18,19]. Leveraging big data science for geochemical feature extraction and information fusion is poised to enhance the efficacy of deep prospecting endeavors in concealed areas [20]. Making full use of the complete characteristics of high-dimensional geochemical data may be the key to achieving a breakthrough in deep prospecting for Carlin-type Au deposits in the Youjiang Basin.

Widely used in various fields, including ore exploration, factor analysis and association rule algorithms play a crucial role in feature extraction and information fusion [21–27]. Specifically, factor analysis is a dimensionality reduction method applied to extract common factors from a group of variables [26,28]. Geologically, it can reduce numerous geochemical variables to a few factors to identify hidden indicators for metallogenic predictions [23–26,28,29]. The association rule algorithm, first proposed by Agrawal et al. [30], refers to the discovery of interesting and frequent patterns, associations, and correlations among items in a database. Strong association rules that meet the minimum support, minimum confidence, and lift thresholds greater than 1 are typically selected for metallogenic predictions based on the local correlation and association of elements within a deposit [21,22,30–34]. Notable distinctions exist between these two methods. Factor analysis elucidates overall correlations or spatial distribution trends among elements, while the association rule algorithm focuses on local correlations or local spatial distribution similarities among elements.

Considering the above disparities, this paper employs the recently discovered Lintan Carlin-type Au deposit in the northern Youjiang Basin as a case study. Situated adjacent to the super-large Lannigou Au deposit (refer to Figure 1), the Lintan Au deposit exhibits promising prospecting potential. Rock samples from the ore-bearing fracture zone and a representative cross-section were systematically collected, and 15 elements in the rock samples, including Au, As, Hg, Sb, Tl, Cu, Pb, Zn, Ag, W, Co, Cd, Ni, Mo, and Bi, were analyzed. Factor analysis and association rule algorithms were jointly used to extract metallogenic information, providing significant exploration vectors and indicators for the Lintan Au deposit.

2. Geological Background

The Youjiang Basin, also referred to as the “Golden Triangle” of Yunnan-Guizhou-Guangxi because of the extensive development of Carlin-type Au deposits, is located at the southwest margin of the Yangtze Craton (Figure 1). The basin underwent three evolutionary stages: a rift basin (Late Early Devonian to Late Devonian), a passive continental margin

(Early Carboniferous to Early Triassic), and a foreland basin (Middle Triassic) [35–37]. Following basin evolution, a super-thick (6–12 km) Paleozoic–Mesozoic marine sedimentary sequence was deposited. This sequence, comprising claystone, siltstone, carbonate rock, and sandstone, predominated over the Proterozoic basement, which consisted of low-grade metamorphosed clastic rocks. Tectonic activities in the Youjiang Basin were chiefly influenced by NNE-ward subduction and collision of the Paleo-Tethys Ocean [38,39], as well as W-ward flat-slab subduction of the Paleo-Pacific plate [40]. These tectonic events resulted in parallel NW-striking and NE-striking fault-and-fold systems in the Youjiang Basin [41,42]. Igneous rocks are absent in the Youjiang Basin and primarily consist of Emeishan flood basalts and shallow volcanic facies diabase (ca. 260 Ma) [43,44], with minor occurrences ultra-mafic (ca. 84 Ma) [45] and quartz porphyry dikes (ca. 100–94 Ma) [46].

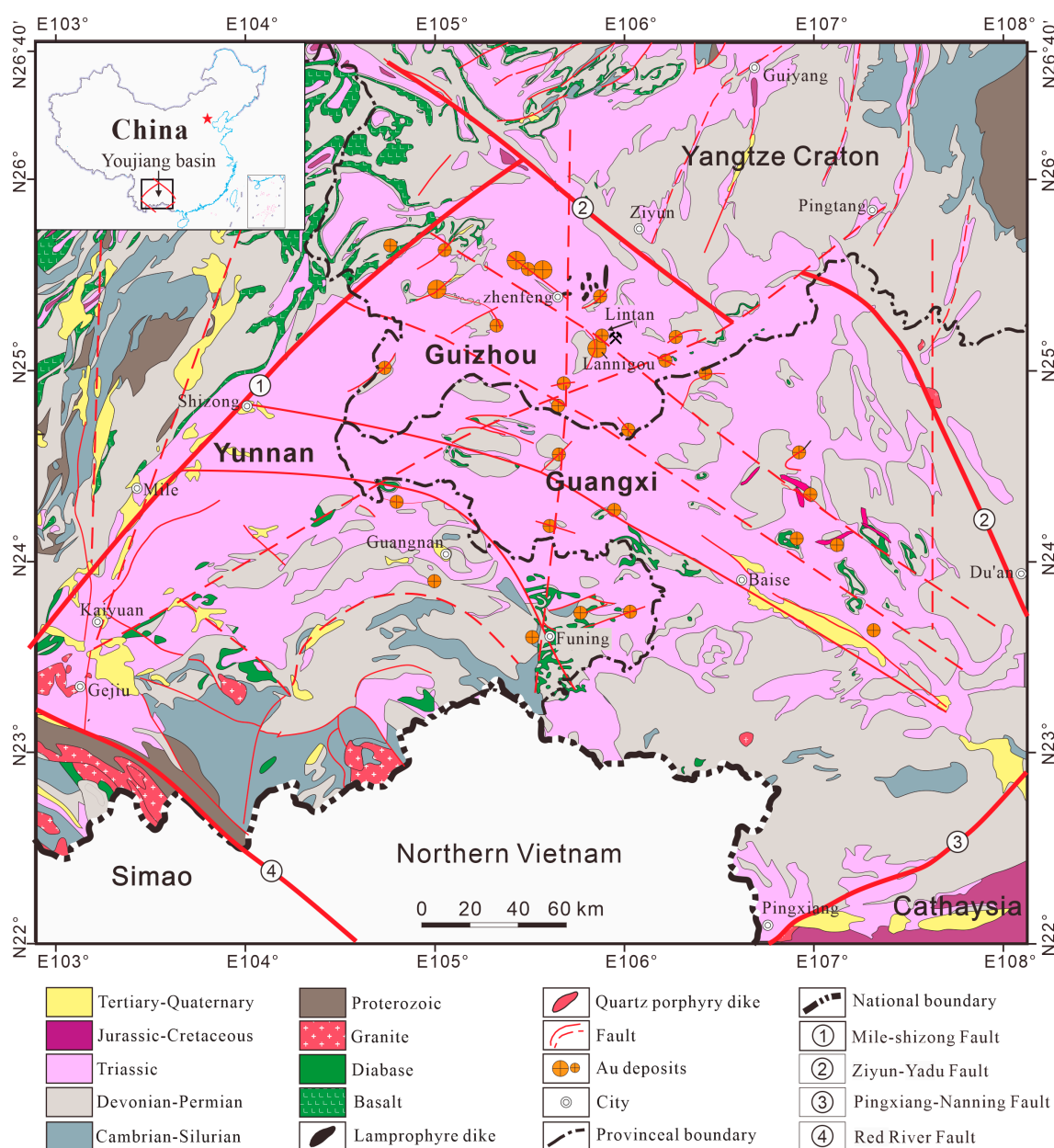


Figure 1. Geological map of the Dian-Qian-Gui “Golden Triangle” region in Southwestern China (modified from Tan et al. [42]).

The Lintan Au deposit is a recently discovered Carlin-type deposit in the northern Youjiang Basin, adjacent to the super-large Lannigou Au deposit (Figure 1). Recent explo-

rations in the Lintan mining area have revealed Au reserves totaling 1.18 t with an average Au grade of 5.61 g/t. The stratigraphic and structural characteristics of the Lintan Au deposit are illustrated in Figure 2, with a concise summary provided below.

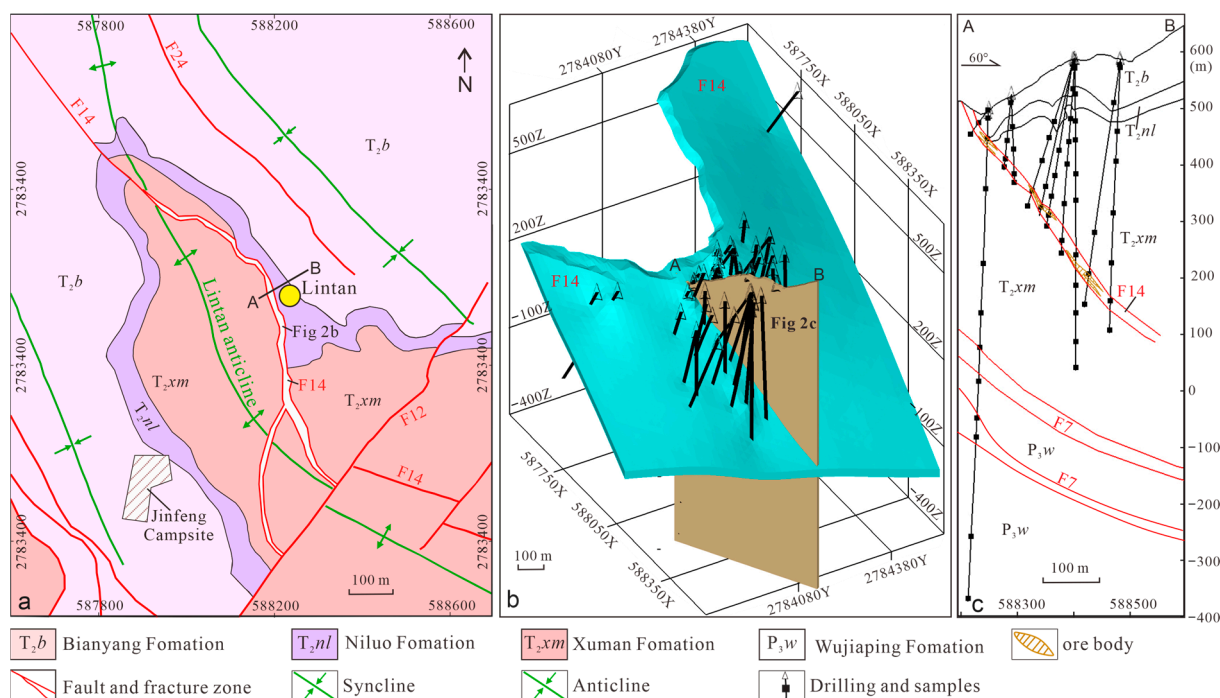


Figure 2. (a) Geological map, (b) three-dimensional map of the ore-bearing F₁₄ fault, and (c) representative A–B profile map of the Lintan Au deposit.

The Lintan mining area mainly consists of Permian shallow-water platform facies carbonate rocks and Triassic deep-water slope facies clastic rocks (Figure 2). The exposed and drilled strata, from shallow to deep, are the Triassic Bianyang, Niluo, and Xuman formations and the Permian Wujiaping Formation. The Bianyang Formation (T_{2by}) is composed of moderately bedded graywacke, fine sandstone, and siltstone interbedded with thin-layered claystone. The Niluo Formation (T_{2nl}) comprises claystone interspersed with thinly layered argillaceous siltstone and nodular limestone. The Xuman Formation (T_{2xm}) consists of thick-bedded to massive claystone, mudstone, limestone, and sandstone. The Wujiaping Formation (P_{3w}) comprises super-thick, dolomitic, bioclastic, and reef limestones.

In the Lintan mining area, the geological formations underwent folding, forming an NW-trending Lintan anticline that is 3000 m long and nearly 700 m wide. This anticline is categorized as a tractive anticline positioned above the gentle F₇ fault, situated between the Wujiaping and Xuman formations. The core of the Lintan anticline primarily comprises rocks from the Xuman Formation, while the SW and NE limbs consist of formations from the Niluo and Bianyang series. The NE limb of the anticline is cut by a series of NW-striking steeply dipping (50–60°) reverse faults (e.g., F₁₄ and F₂₄), which are cut by younger NE-striking high-angle strike-slip faults (e.g., F₁₂). Au orebodies commonly occur as veins and lenses in the steeply dipping F₁₄ fault and are hosted in the calcareous siltstone, sandstone, and mudstone of the Xuman Formation. The average thickness of the orebodies is approximately 2.2 m, with a vertical continuity of approximately 600 m.

Au mineralization within the Lintan deposit exhibits a close association with several geological processes, including decarbonatization, silicification, sulfidation, argillization, and dolomitization, like other Carlin-type deposits found in Nevada, USA, and the Youjiang Basin, China [1,47]. Predominantly, ore minerals consist of sulfides formed through sulfidation, comprising arsenian pyrite and arsenopyrite, with lesser occurrences of orpiment, realgar, and stibnite. Au primarily resides within arsenian pyrite and arsenopyrite

in invisible forms (e.g., nanoparticles and crystal lattice Au). Gangue minerals comprise calcite, quartz, dolomite, and clay minerals (e.g., illite), commonly filling fractures at the periphery of highly porous decarbonated rocks that host high-grade orebodies.

3. Sampling and Analyses

A total of 125 rock samples, each weighing approximately 500 g, were collected from the F₁₄ fault fracture zone and a representative A–B cross-section at the Lintan deposit. The detailed sampling locations are shown in Figure 2. The samples were cleaned, dried, crushed, and ground to a size of <200 mesh for subsequent chemical analysis.

Rock samples were analyzed at the Geological Experimental Testing Center of Hubei Province, China, and the contents of 15 elements, namely Au, As, Hg, Sb, Tl, Cu, Pb, Zn, Ag, W, Co, Cd, Ni, Mo, and Bi, were determined. The contents of Bi, Co, Cu, Mo, Ni, Pb, Sb, Tl, W, and Zn were analyzed through Inductively Coupled Plasma Mass Spectrometry (ICP-MS), while Atomic Fluorescence Spectrometry (AFS) was employed for As and Hg analysis. The content of Ag was determined using Alternating Current Arc Emission Spectrometry (AC-AES), while the Au content was analyzed using activated carbon adsorption coupled with Inductively Coupled Plasma-Atomic Emission Spectrometry (ICP-AES). The detection limits are listed in Table 1. During the testing process, the national primary standard reference materials from China were used for accuracy testing, resulting in a 100% pass rate. Additionally, six random rock samples that were selected for repeatability testing achieved a 100% pass rate.

Table 1. Statistical parameters of elements in rock samples from the Lintan deposit.

Parameters	Au	Ag	As	Bi	Cd	Co	Cu	Hg	Mo	Ni	Pb	Sb	Tl	W	Zn
DL	0.2	0.01	0.2	0.03	0.02	0.1	0.1	0.0005	0.12	1	0.2	0.03	0.05	0.3	1
Average	290	0.08	436	0.36	0.18	15.4	33.2	0.42	0.44	29.6	22.1	3.13	0.68	1.66	80.6
Median	8.2	0.07	29.3	0.35	0.15	15.2	32.5	0.28	0.30	29.1	18.9	1.93	0.70	1.61	80.5
Minimum	1.1	0.01	1.61	0.06	0.07	1.02	1.2	0.063	0.13	6.23	3.4	0.31	0.09	0.11	8.64
Maximum	9615	0.39	4473	1.17	0.97	29.5	107	4.99	2.81	56.2	107	39.7	1.10	3.13	132
Std	0.85	0.05	0.91	0.03	0.03	0.03	0.04	0.35	0.08	0.01	0.06	0.16	0.02	0.02	0.02
Skewness	1.22	−0.34	0.34	−1.12	1.89	−4.09	−3.72	0.57	1.13	−2.27	0.32	0.26	−3.12	−5.17	−4.3
Kurtosis	0.47	6.37	−1.25	5.84	6.42	23.4	24.0	0.83	1.38	11.9	1.67	−0.24	17.01	37.9	24
CV	3.52	0.68	1.83	0.37	0.75	0.26	0.35	0.64	1.01	0.23	0.72	1.34	0.22	0.21	0.21

Note: The unit of Au is ng/g and other elements are µg/g. DL is Detection limit, Std is Standard Deviation, and CV is Coefficient of Variation.

4. Results

4.1. Statistical Characteristics

The statistical parameters of the 15 elements in the rock samples from the Lintan deposit are listed in Table 1 and shown in Figure 3a. The raw data (see Supplementary Materials) were log-transformed before calculating the standard deviation, skewness, kurtosis, and coefficient of variation. The Au content was 1.1–9615 ng/g, with a mean of 290 ng/g, median of 8.2 ng/g, skewness of 1.22, kurtosis of 0.47, and variation coefficient of 3.52. These metrics reflect a log-normal distribution with a right-skewed trend, flat peak shape, and a wide variation range.

Among other elements, those with skewness values above 0, such as, Hg, Sb, Cd, Mo, and Pb, exhibit a right-skewed trend. In contrast, elements like Ag, Bi, Co, Cu, Ni, Tl, W, and Zn, with skewness values below 0, display a left-skewed trend. Additionally, elements with kurtosis above 5, including Ag, Bi, Cd, Co, Cu, Ni, Tl, W, and Zn, present a steep peak shape. Elements with kurtosis ranging from 0 to 5, such as Hg, Mo, and Pb, feature a moderately steep peak shape. Lastly, elements with kurtosis below 0, like As and Sb, demonstrate a flat peak shape. Moreover, As, Hg, Sb, and Mo had variation coefficients above 1, indicating a large variation range. Ag, Cd, Hg, and Pb had variation coefficients between 0.5 and 1, showing a moderate variation range, while Bi, Co, Cu, Ni, Tl, W, and Zn had variation coefficients below 0.5, indicating a narrow variation range.

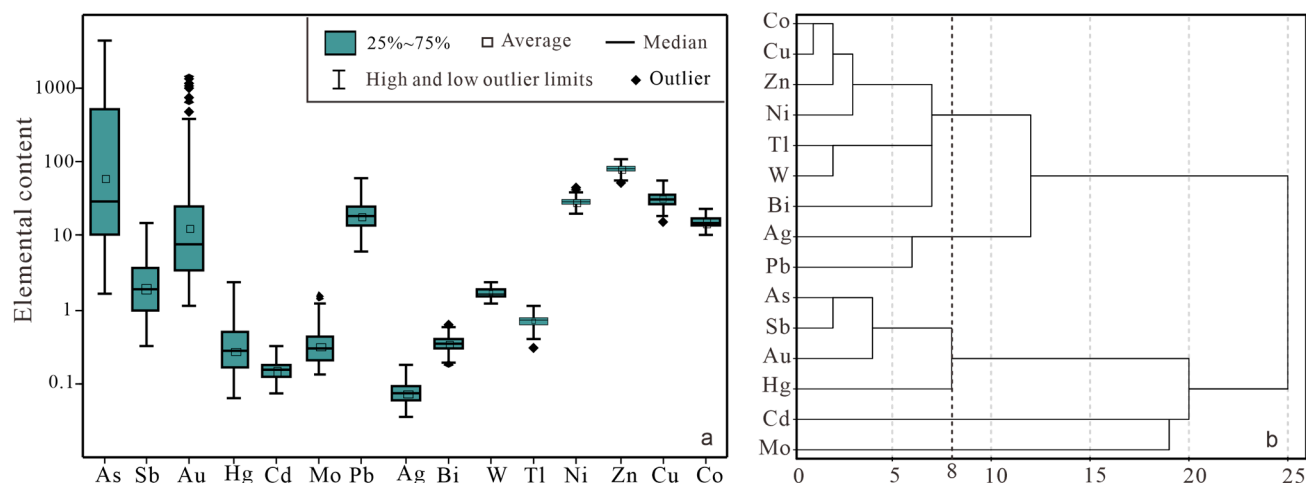


Figure 3. (a) Box plots of 15 elements; (b) Dendrogram of the R-cluster analysis of the 15 elements.

Correlation and R-type cluster analyses were conducted using SPSS Statistics Software (IBM Corp., Armonk, NY, USA) based on log-transformed data, and the results are presented in Table 2 and Figure 3b, respectively. As depicted in Figure 3b, with the distance coefficient set to 8, the 15 elements can be classified into five distinct groups, each displaying strong internal correlations. The first group encompasses Co, Cu, Zn, Ni, Tl, W, and Bi, with correlation coefficients ranging from 0.53 to 0.86. In the second group, Pb and Ag exhibit a correlation coefficient of 0.69. The third group comprises Au, As, Hg, and Sb, demonstrating correlation coefficients spanning from 0.57 to 0.81. The fourth and fifth groups consist of Cd and Mo, respectively. Notably, Ag and Pb also display strong positive correlations with Bi, Co, and Cu, with correlation coefficients ranging from 0.50 to 0.70. Thus, the elements in the first and second groups can be combined into a new group with a distance coefficient of approximately 12.

Table 2. Correlation matrix of elements in rock samples from the Lintan deposit.

Elements	As	Sb	Au	Hg	Cd	Mo	Pb	Ag	Bi	W	Tl	Ni	Zn	Cu	Co
As	1														
Sb	0.81	1.00													
Au	0.79	0.69	1.00												
Hg	0.56	0.70	0.59	1.00											
Cd	0.06	0.31	0.06	0.39	1.00										
Mo	0.12	0.34	0.09	0.28	0.26	1.00									
Pb	0.03	0.02	0.01	−0.20	−0.25	0.40	1.00								
Ag	0.13	0.18	0.11	−0.01	−0.32	0.28	0.69	1.00							
Bi	0.05	0.02	0.01	−0.25	−0.40	0.10	0.54	0.61	1.00						
W	0.29	0.24	0.22	0.03	−0.37	0.05	0.33	0.46	0.69	1.00					
Tl	0.39	0.47	0.34	0.22	−0.13	0.18	0.28	0.43	0.64	0.81	1.00				
Ni	0.20	0.05	0.11	−0.14	−0.33	0.03	0.35	0.37	0.56	0.64	0.59	1.00			
Zn	0.27	0.09	0.18	−0.02	−0.46	0.07	0.44	0.49	0.58	0.71	0.53	0.80	1.00		
Cu	0.22	0.18	0.11	−0.03	−0.47	0.15	0.50	0.70	0.73	0.73	0.68	0.69	0.79	1.00	
Co	0.22	0.09	0.11	−0.13	−0.53	0.14	0.53	0.66	0.71	0.68	0.60	0.84	0.83	0.86	1

4.2. Spatial Distribution of Elements

Figures 4 and 5 display the spatial distributions of single elements in the A-B cross-section and F₁₄ fault of the Lintan deposit, respectively. The interpolation method of Figures 4 and 5, as well as subsequent spatial distribution maps, is inverse distance square weighting. Figure 6 shows the vertical variations in the 15 elements of the F₁₄ fault. Eleven color grades based on the percentiles of the raw data (Table 3) were used to display the enrichment or depletion of elements.

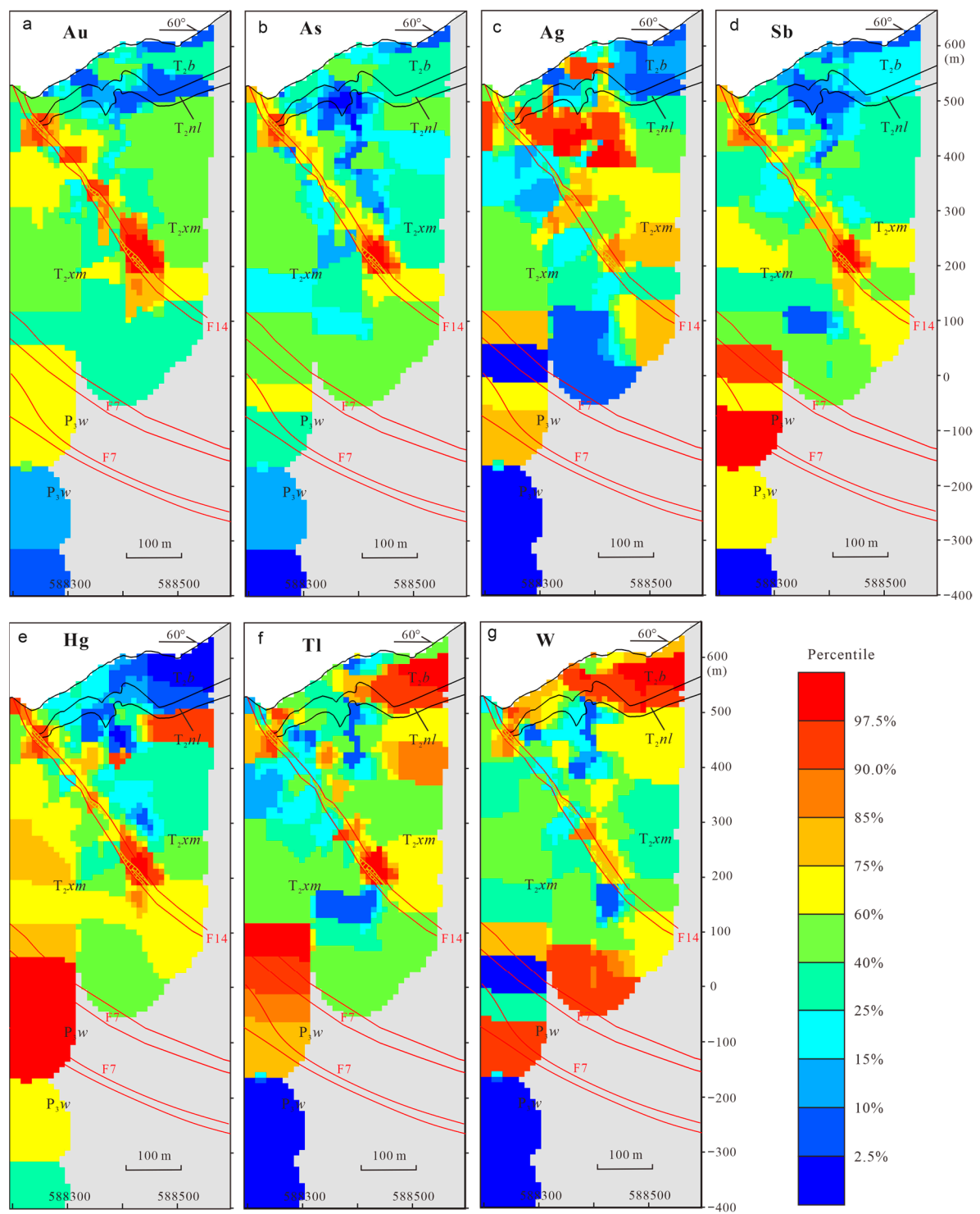


Figure 4. Cont.

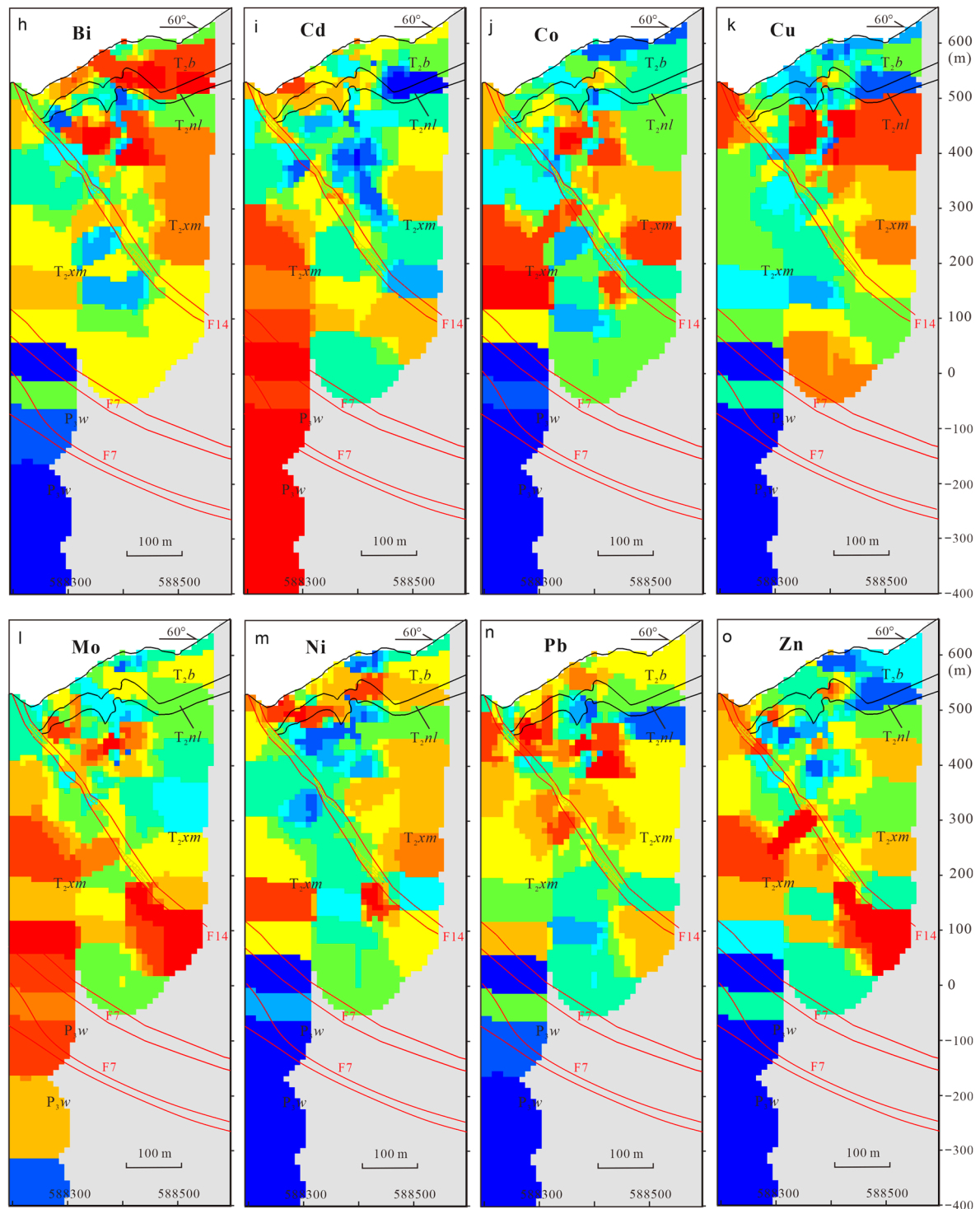


Figure 4. Spatial distributions of 15 elements (a–o) in the A–B cross-section.

In Figure 4a, areas with high Au content ($\geq 75\%$, orange to deep red) were mainly located in the F₁₄ fault, corresponding to strong Au mineralization (Figure 2c). Analogously, rocks containing Au content ranging from 11.5 to 39.8 ng/g (60%–75%, yellow), indicative of weak Au mineralization, were found distributed within or along the periphery of the F₁₄ and F₇ faults. The spatial distributions of As, Ag, Sb, Hg, Tl, and W (Figure 4b–g) were comparable to those of Au, although some significant differences existed. The F₇ faults and their vicinity demonstrated intense Sb, Hg, Tl, and W anomalies (orange to deep red). Additionally, local positions in the Xuman and Bianyang formations above the

F₁₄ fault also showed high contents of Ag, Hg, Tl, and W (Figure 4c–g). Other elements displayed markedly different spatial distributions than Au (Figure 4h–o). Areas with high contents of Bi, Co, Cu, Ni, Pb, and Zn were primarily distributed outside the F₁₄ fault in the Xuman, Niluo, and Bianyang formations. However, Cd (Figure 4i) and Mo (Figure 4l) mainly displayed intense anomalies in the Wujiaping Formation and the nearby Xuman Formation, particularly within and at the periphery of the F₇ fault.

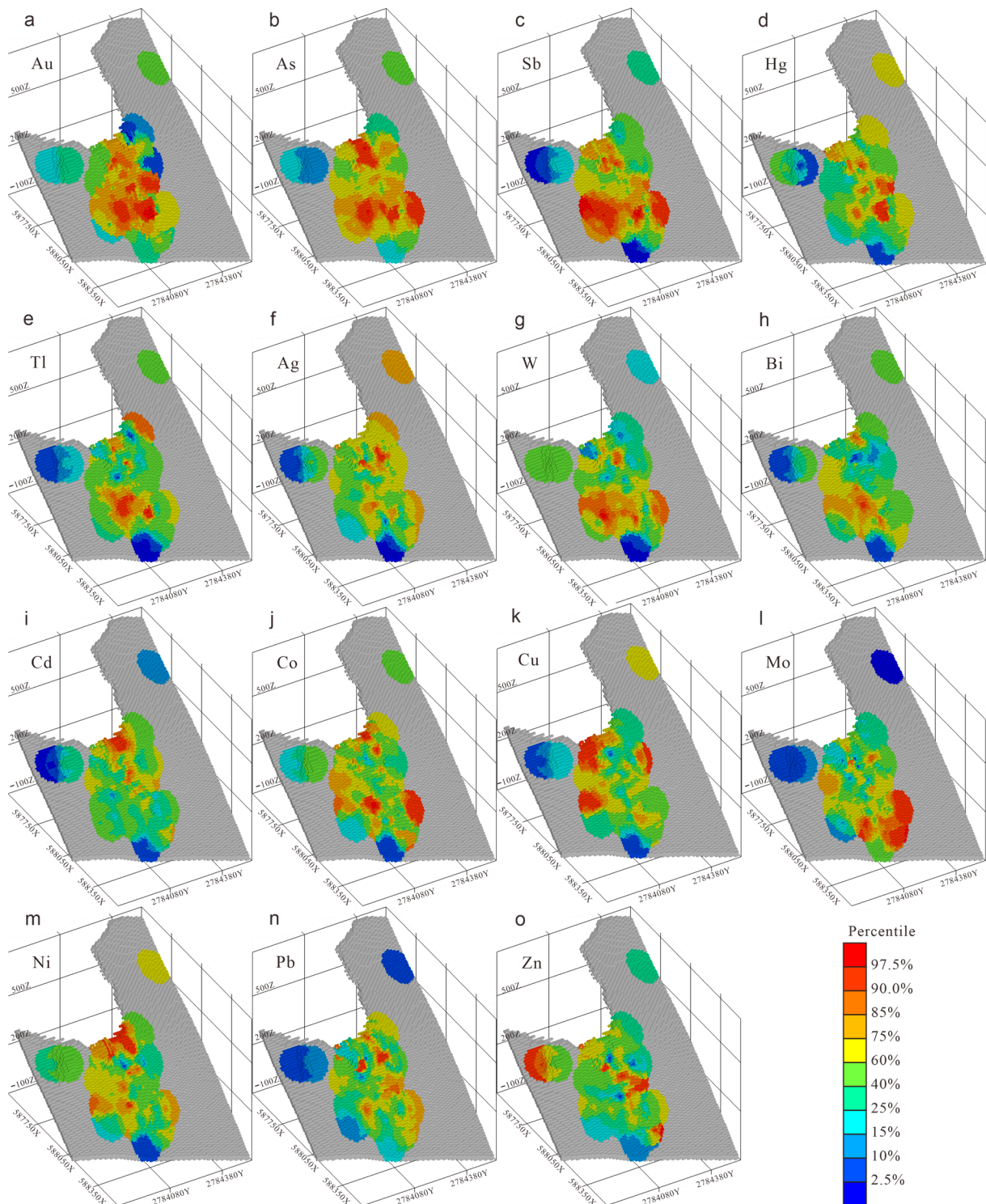


Figure 5. Spatial distributions of 15 elements (a–o) in the F₁₄ fault.

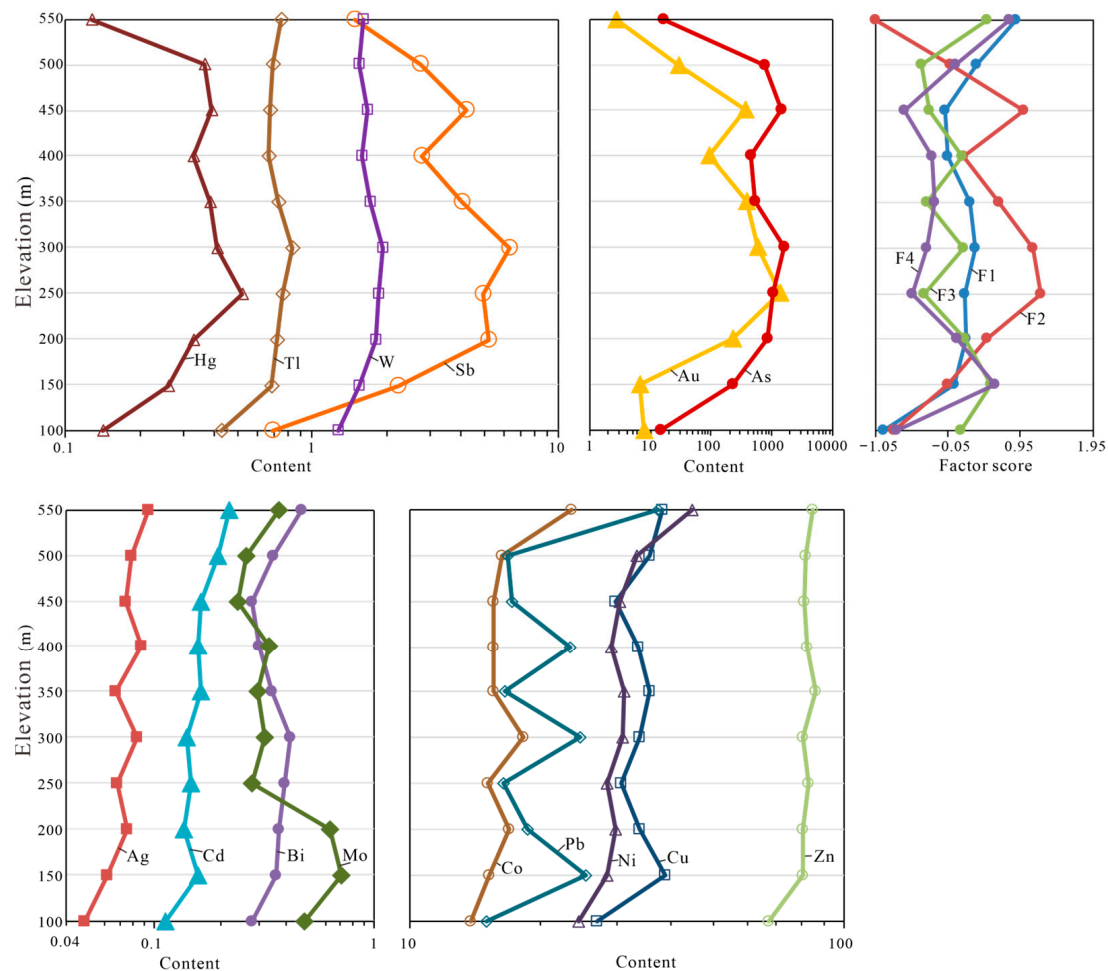


Figure 6. Vertical variations in 15 elements from the F₁₄ fault.

Table 3. Percentiles of elements and factor scores.

Percentiles	Au	Ag	As	Bi	Cd	Co	Cu	Hg	Mo	Ni	Pb	Sb	Tl	W	Zn	F1	F2	F3	F4
97.5%	2570	0.26	2904	0.66	0.64	23.6	57.3	1.61	1.71	47.2	62.9	10.2	0.93	2.29	106	1.20	1.95	2.57	2.69
90%	739	0.11	1362	0.49	0.23	19.3	43.4	0.73	0.78	35.9	34.2	6.87	0.86	2.10	97.6	0.71	1.55	0.99	0.89
85%	282	0.10	1063	0.44	0.21	18.3	39.5	0.58	0.60	34.9	31.4	5.17	0.83	1.96	93.1	0.61	1.22	0.66	0.72
75%	39.8	0.09	520	0.40	0.18	17.1	37.7	0.51	0.47	32.1	25.5	3.74	0.78	1.83	91.0	0.45	0.79	0.48	0.39
60%	11.5	0.08	113	0.37	0.16	16.4	34.6	0.35	0.34	30.2	19.9	2.54	0.74	1.67	85.2	0.26	0.03	0.09	0.07
40%	6.02	0.07	16.0	0.33	0.14	14.5	31.1	0.23	0.27	28.2	16.3	1.48	0.65	1.56	78.4	0.00	−0.48	−0.30	−0.31
25%	3.80	0.06	10.6	0.29	0.12	13.5	27.6	0.16	0.21	25.9	13.4	1.00	0.59	1.51	74.1	−0.21	−0.80	−0.63	−0.52
15%	3.10	0.05	7.34	0.27	0.11	12.4	24.0	0.11	0.18	24.9	11.8	0.74	0.55	1.43	69.9	−0.45	−1.00	−0.88	−0.71
10%	2.74	0.04	5.11	0.23	0.10	11.7	22.0	0.10	0.17	23.6	10.1	0.63	0.51	1.38	64.3	−0.71	−1.14	−0.95	−1.01
2.5%	1.70	0.03	2.78	0.17	0.08	7.64	14.8	0.08	0.14	18.3	7.85	0.42	0.32	1.04	35.0	−1.62	−1.37	−1.45	−1.52

In Figure 5a, several areas exhibiting high Au content (ranging from orange to deep red) are observed scattered across the central and shallow regions of the F₁₄ fault, with elevations approximately around 250 m and 450 m, respectively. Similarly, elements such as As, Sb, Hg, Tl, and W demonstrate similar characteristics to Au, with their high-content sites primarily concentrated at elevations of 200–300 m and 400–500 m. Areas with a high Bi content are predominantly found at elevations of 150–300 m and 550 m, indicating localized similarities with Au distribution. Notably, molybdenum exhibits high content along the depth of the F₁₄ fault, at elevation of 100–200 m. Conversely, the contents of Ag, Cd, and Ni gradually rose from deep to shallow and showed the highest values at a shallow altitude of 550 m. Lastly, the spatial distributions of Pb, Zn, Co, and Cu were disordered and scattered, which were significantly different from those of Au.

4.3. Factor Analysis

Factor analysis is a statistical method used to analyze the correlation between multiple variables and reduce them to fewer factors [26,28]. Its advantages include simplifying data, improving analysis efficiency, exploring data structures and patterns, and constructing reliable indicator systems [48]. Before conducting the factor analysis, it was imperative to perform the Kaiser–Meyer–Olkin (KMO) measure of sampling adequacy and Bartlett’s test of sphericity. The value of KMO should be greater than 0.6, and the *p*-value of Bartlett’s test should be less than 0.05, indicating a correlation between elements [49]. This meets the requirements of factor analysis and confirms the significance of its effect [23,28,50].

Factor analysis was performed using SPSS Statistics Software (IBM Corp., Armonk, NY, USA) based on the log-transformed data of 15 elements in the rock samples from the Lintan deposit. The KMO value was 0.803, and the *p*-value of Bartlett’s test was 0.000, meeting the requirements of factor analysis and yielding significant results. Four factors were extracted using principal component analysis with a cumulative contribution rate of variance greater than 80%. The rotated component matrix of the elements is listed in Table 4 and shown in Figure 7. The Kaiser normalizing maximum variance method was used for rotation, and the rotation converged after six iterations.

Table 4. Rotated loading coefficient matrix of the 15 elements.

Elements	F1	F2	F3	F4
W	0.87	0.16	0.07	−0.03
Ni	0.85	0.00	0.08	−0.13
Tl	0.83	0.31	0.05	0.23
Cu	0.82	0.08	0.39	−0.13
Co	0.82	0.03	0.40	−0.23
Zn	0.80	0.11	0.24	−0.25
Bi	0.75	−0.13	0.38	−0.05
As	0.18	0.91	0.02	−0.07
Au	0.08	0.90	0.03	−0.12
Sb	0.13	0.87	0.08	0.32
Hg	−0.07	0.77	−0.09	0.35
Pb	0.28	−0.08	0.86	−0.01
Ag	0.43	0.09	0.77	−0.08
Cd	−0.35	0.17	−0.24	0.77
Mo	0.02	0.14	0.57	0.66
Eigenvalue	6.42	3.35	1.48	0.87
% of variance	34.6	21.4	14.9	9.85
Cumulative %	34.6	56.0	70.9	80.8

Note: The absolute value of loading coefficient greater than 0.3 are bold.

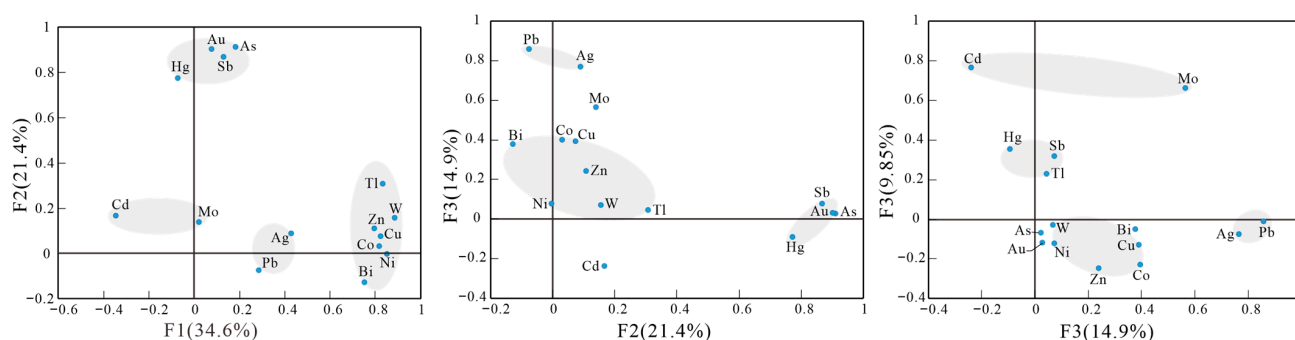


Figure 7. Diagram of factor loading coefficients.

Factor 1 (F1) explained 35% of the dataset total variance and had high positive loading coefficients for W (0.89), Ni (0.85), Tl (0.83), Cu (0.82), Co (0.82), Zn (0.80), and Bi (0.75), which was consistent with the first group of elements obtained by cluster analysis. Additionally, F1 displayed a moderately positive loading coefficient for Ag (0.43) and a negative

loading coefficient for Cd (-0.35). Conversely, Factor 2 (F2) with 21% of the total variance, showed high positive loading coefficients for As (0.91), Au (0.90), Sb (0.87), and Hg (0.77), similar to the third group of elements obtained by cluster analysis. Notably, F2 also had a weak positive loading of Tl (0.31), which is an ore-related element. Factor 3 (F3) exhibiting a percentage explained variable of 15%, had high positive loading coefficients for Pb (0.86), Ag (0.77), and Mo (0.57) and weak positive loading coefficients for Cu (0.39), Co (0.40), and Bi (0.38), resembling the second group elements of cluster analysis. Similarly, Factor 4 (F4) with 10% of explained variance, had high positive loadings for Cd (0.77) and Mo (0.66) and weak positive loadings for Sb (0.32) and Hg (0.35).

The spatial distributions of the four factors in the A–B cross-section and F_{14} fault are presented in Figures 8 and 9, respectively. The vertical variations in factor scores of the F_{14} fault are shown in Figure 6. In the A–B cross-section, areas with high F1 scores (orange to deep red) were mainly distributed in the Xuman, Niluo, and Bianyang formations. The high-scoring areas of F2 were in the F_{14} and F_7 faults, corresponding to the sites of intense Au mineralization. Areas with high F3 scores were mostly distributed in the Xuman, Niluo, and Bianyang formations at the periphery of the F_{14} and F_7 faults. Finally, F4 displayed high scores near the contact areas of the Wujiaping and Xuman formations, particularly within and at the periphery of the F_7 fault.

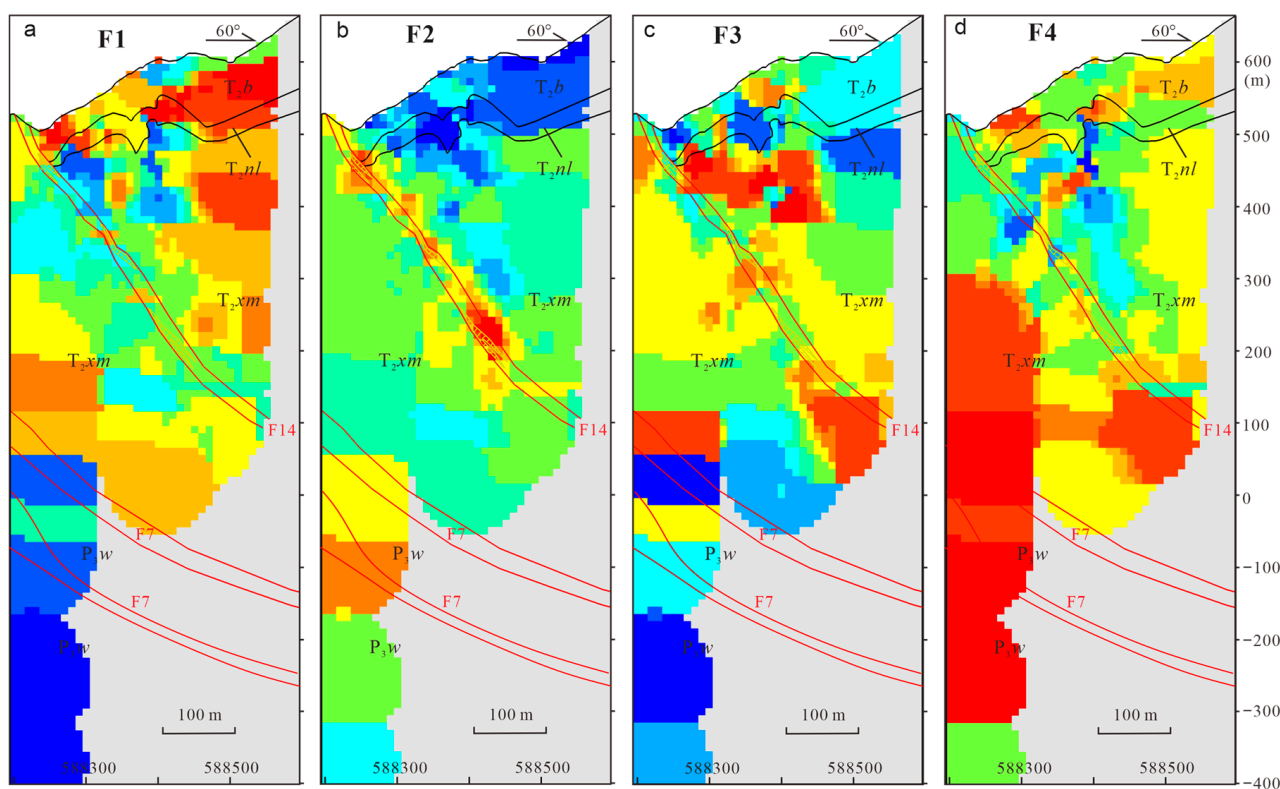


Figure 8. Spatial distributions of factor scores (a–d) in the A–B cross-section.

In the F_{14} fault, the high-scoring areas of F1 were primarily situated in the south-central and superficial areas at elevations of 250–350 m and 480–550 m. The spatial distribution of F2 was highly consistent with the distribution of Au and was mainly located in the central area of the F_{14} fault at elevations of approximately 250–300 and 450 m. F3 mainly showed high scores in deep areas with elevations of 100–200 m, followed by shallow areas with elevations of approximately 400 m and 500 m. F4 had high scores in the shallow and deep regions, with elevations of 100–200 m to 500–550 m.

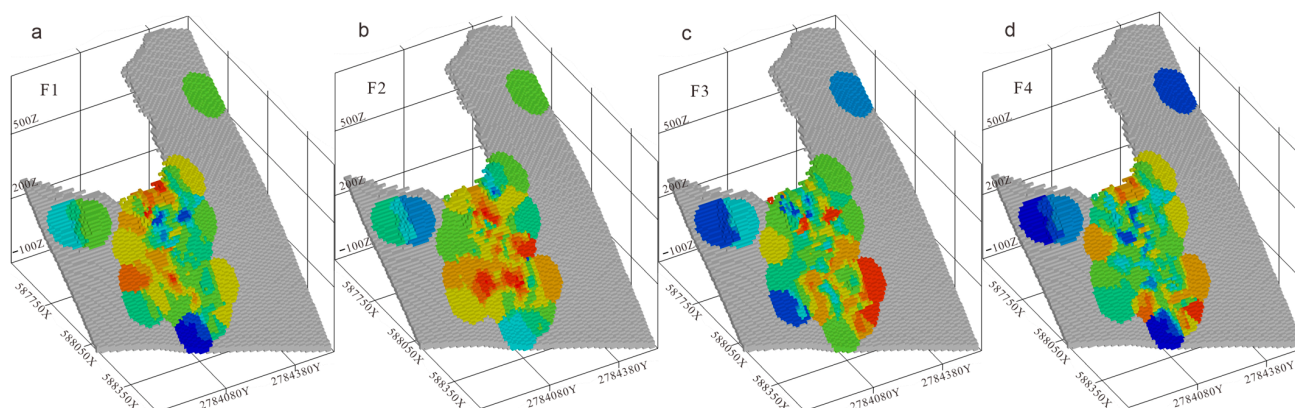


Figure 9. Spatial distributions of factor scores (a–d) in the F_{14} fault.

4.4. Association Rule Algorithm

The association rule algorithm, a method for uncovering significant relationships between items within a dataset, reflects the interdependence and association among these items [30,48]. Implemented through SPSS Modeler Software (IBM Corp., Armonk, NY, USA), the Apriori algorithm is employed for this purpose. This process comprises two primary steps: identifying frequent item sets and generating robust association rules. These association rules typically employ metrics such as support, confidence, and lifting to gauge and filter out rules that satisfy specific conditions [21,22,30,32,34]. The association rules are expressed as $A \rightarrow B$, where A and B are disjointed. Support is the probability of A and B occurring simultaneously, i.e., $\text{support}(A \rightarrow B) = P(A \cap B)$. Confidence refers to the probability of B occurring under the condition that A occurs, i.e., $\text{confidence}(A \rightarrow B) = P(B|A)$. Lift reflects whether the rule has a gain, which is the ratio of the probability of B occurring under the condition of A occurring relative to the total probability of B occurring, i.e., $\text{lift}(A \rightarrow B) = P(B|A)/P(B)$. Rules that satisfy the minimum support and confidence are strong association rules. After obtaining the strong association rules, a lift was used to determine whether the strong association rules were valid. If the lift of $A \rightarrow B < 1$, this indicates that the rule is negatively correlated and has no gain. Conversely, if the lift of $A \rightarrow B > 1$, this indicates that the rule is positively correlated and has a gain.

The high- and low-outlier limits of the 15 elements in rock samples from the Lintan deposit were determined from box plots (Figure 3a) using log-transformed data. The data falling within the limits of high and low outliers underwent k-means clustering, resulting in three distinct groups: high, medium, and low. Automatically, data surpassing the high-outlier limit were categorized as high content, while those falling below the low-outlier limit were classified as low content. Specifically, Au was categorized into three groups: low content (Au1), consisting of 40 samples ranging from 1.1 to 4.5 $\mu\text{g/g}$; medium content (Au2), comprising 58 samples ranging from 4.5 to 69.2 $\mu\text{g/g}$; and high content (Au3), encompassing 27 samples ranging from 69.2 to 9615 $\mu\text{g/g}$.

Table 5 lists the clustering results for the 15 elements. Au serves as the primary ore-forming and target element. Its low-content category (Au1) signifies the absence of mineralization, while its medium-content category (Au2) indicates weak mineralization. Conversely, its high-content category (Au3) represents significant mineralization. The probability of randomly selecting a sample from the dataset was 32.0% for Au1, 46.4% for Au2, and 21.6% for Au3.

Association rule analysis was performed using Au as the target and other elements as inputs. Table 6 displays 12 representative rules generated with a minimum support of 2%, a minimum confidence of 80%, a minimum lift of 1, and a maximum of seven antecedents. Rules 1, 6, and 9 are described as follows.

Table 5. K-means clustering results for elements.

Element	Categories	Range	Numbers	Element	Categories	Range	Numbers
Au	Au1	[1.1, 4.5)	40	Ag	Ag1	[0.01, 0.06)	35
	Au2	[4.5, 69.2)	58		Ag2	[0.06, 0.08)	43
	Au3	[69.2, 9615]	27		Ag3	[0.08, 6.37]	47
As	As1	[1.61, 33.1)	64	Bi	Bi1	[0.06, 0.29)	29
	As2	[33.1, 339)	27		Bi2	[0.29, 0.41)	67
	As3	[339, 4473]	34		Bi3	[0.41, 1.17]	29
Cd	Cd1	[0.07, 0.13)	33	Co	Co1	[1.02, 14.1)	41
	Cd2	[0.13, 0.19)	62		Co2	[14.1, 17.8)	58
	Cd3	[0.19, 0.97]	30		Co3	[17.8, 29.5]	26
Cu	Cu1	[1.20, 28.2)	35	Hg	Hg1	[0.06, 0.20)	44
	Cu2	[28.2, 39.8)	72		Hg2	[0.20, 0.48)	47
	Cu3	[39.8, 107]	18		Hg3	[0.48, 4.99]	34
Mo	Mo1	[0.13, 0.26)	47	Ni	Ni1	[6.23, 27.5)	42
	Mo2	[0.26, 0.52)	50		Ni2	[27.5, 33.1)	60
	Mo3	[0.52, 2.81]	28		Ni3	[33.1, 56.2]	23
Pb	Pb1	[3.40, 15.1)	42	Sb	Sb1	[0.31, 1.24)	45
	Pb2	[15.1, 26.9)	57		Sb2	[0.52, 3.61)	48
	Pb3	[26.9, 107]	26		Sb3	[3.61, 39.7]	32
Tl	Tl1	[0.09, 0.62)	35	W	W1	[0.11, 1.51)	31
	Tl2	[0.62, 0.78)	55		W2	[1.51, 1.82)	62
	Tl3	[0.78, 1.1]	35		W3	[1.82, 3.13]	32
Zn	Zn1	[8.64, 70.8)	21				
	Zn2	[70.8, 87.1)	64				
	Zn3	[87.1, 132]	40				

Table 6. Representative association rules.

Number	Association Rules	Support (%)	Confidence (%)	Lift
Rule 1	Ag1-As1 → Au1	16.8	95.2	2.98
Rule 3	Tl1-Sb1-As1-Ag1 → Au1	9.60	100	3.13
Rule 2	Cu1-Ag1-Sb1 → Au1	10.4	100	3.13
Rule 4	Bi1-Cu1-Co1-Sb1-Mo1 → Au1	6.40	100	3.13
Rule 5	Mo3-Pb2-Bi2 → Au2	7.20	100	2.16
Rule 6	As2-Hg2-Tl2-W2 → Au2	4.80	100	2.16
Rule 7	Cu3-Bi3-As1 → Au2	6.40	100	2.16
Rule 8	Hg2-Ag2-Tl2-Cd2 → Au2	6.40	100	2.16
Rule 9	Tl3-As3-Ag2 → Au3	8.00	100	4.63
Rule 10	Sb3-W3-Tl3-As3-Ni2 → Au3	8.00	100	4.63
Rule 11	Ni2-Tl3-As3-Cu2 → Au3	8.00	100	4.63
Rule 12	W3-Tl3-As3-Zn3-Ni2-Cd2 → Au3	5.60	100	4.63

Rule 1 (Ag1-As1→Au1) indicates that when the samples have contents of Ag1 and As1, the probability of Au contents being Au1 is 95.2%, which is 2.98 times the normal occurrence probability of Au1 samples. The opposite event of Rule 1 occurs when the samples do not contain Ag1 and As1; the probability of the Au contents being Au2 or Au3 in the samples is 95.2%. Rule 6 (As2-Hg2-Tl2-W2→Au2) indicates that when the samples show contents of As2, Hg2, Tl2, and W2, the probability of Au contents being Au2 is 100%, which is 2.16 times the normal occurrence probability of Au2 samples. Rule 9 (Tl3-As3-Ag2 → Au3) indicates that when the samples have contents of Tl3, As3, and Ag2, the probability of Au contents being Au3 is 100%, which is 4.63 times the normal occurrence probability of Au3 samples.

5. Discussion

5.1. Control Mechanisms of Element Spatial Distributions

Elements controlled by the same geological processes tend to have similar spatial distribution patterns [51]. Factor analysis can extract the primary information from a geochemical dataset as fewer factors that can be interpreted in terms of various geological processes [24–26]. Factor analysis of the 15 element contents from rock samples obtained from the Lintan deposit revealed the extraction of four distinct factors. This suggests that the spatial distributions of these elements exhibit four distinct patterns controlled by varying mechanisms.

Elements in F1 (W, Ni, Tl, Cu, Co, Zn, and Bi) were primarily enriched in the Bianyang, Xuman, and Niluo formations (Figure 8a) and relatively depleted in the ore-bearing F₁₄ and F₇ faults, indicating that F1 was mainly controlled by sedimentary diagenesis and represented the background characteristics of the strata. Notably, W and Tl also exhibited weak positive correlations with the ore-related elements of Au, As, Sb, and Hg, with correlation coefficients of 0.22–0.47 and an average of 0.28 (Table 2). Tan et al. [52], Li et al. [11], and Hu, et al. [53] reported that Tl and W are also closely associated with Carlin-type Au mineralization in the Youjiang Basin, showing geochemical halos consistent with Au, As, Sb, and Hg. Therefore, although the spatial distribution of W and Tl was mainly controlled by sedimentary diagenesis, it was likely partially influenced by Au metallogenic activities and displayed high contents in the F₁₄ and F₇ faults (Figure 4f,g).

F2 exhibited notably high positive loading coefficients for Au, As, Sb, and Hg, all of which are recognized as metallogenic elements in Carlin-type deposits. The close correlation among the Au, As, Sb, and Hg result from the precipitation of sulfide minerals (e.g., arsenian pyrite, arsenopyrite, orpiment, realgar, and stibnite) in ore during Au mineralization. The areas with high scores in F2 were predominantly concentrated around the F₁₄ and F₇ faults (refer to Figure 8b) and showed relatively low concentrations in the Bianyang, Xuman, and Niluo formations. Therefore, F2 is indicative of Au mineralization. Furthermore, Tl demonstrated a weak positive loading coefficient (0.31) in F2 (refer to Table 4), emphasizing its minor contribution during Au mineralization.

F3 exhibited high positive loading coefficients for Pb, Ag, and Mo. While the high-scoring areas of F3 were primarily situated within the Xuman Formation, they were mainly distributed in the vicinity of the F₁₄ and F₇ faults (refer to Figure 8c), displaying an exceptional peripheral halo of Au mineralization. In addition, F3 had a weak positive loading of Cu, Co, and Bi, which had a high background in the Bianyang, Xuman, and Niluo formations. These results suggest that F3 was mainly controlled by ore-forming hydrothermal activity, although it was partly influenced by sedimentary diagenesis.

F4 (Cd and Mo) showed high scores in the contact zone between the Wujiaping and Xuman formations, particularly in the F₇ fault (Figure 8d), demonstrating a large hydrothermal alteration zone surrounding the F₇ fault. Structurally, the contact zone between the Wujiaping and Xuman formations is a regional unconformity interface [54], which easily undergoes large-scale tectonic sliding during subsequent tectonic activities, resulting in large tectonic fracture zones (e.g., F₇ fault). Upwelling deep ore-forming hydrothermal fluids usually preferentially crowd into regional fracture zones and alter the surrounding rocks [52]. Combining the weak positive loading coefficients of Sb, Hg, and Tl on F4 (Table 4), it appears that F4 was also likely controlled by ore-forming hydrothermal activity.

5.2. Exploration Vectors

Geochemical exploration is one of the most direct methods for prospecting hydrothermal metal deposits [16,17,55]. This is commonly achieved by systematically measuring the elemental composition and spatial distribution of natural substances at different scales, studying their dispersion, migration, enrichment, and evolution, and then delineating geochemical anomalies related to mineralization [16,17]. Moreover, the two- or three-dimensional spatial distributions of elements at the deposit scale have been used to trace the migration channels and precipitation spaces of ore-forming fluids [52,56–58].

In the A-B cross-section of the Lintan Au deposit (Figure 4), areas with high contents (orange to deep red) of Au, As, Sb, Hg, and Tl were mainly distributed in the ore-bearing F₁₄ fault. If the Au anomaly threshold (4.5 ng/g) was set to three times the average Au content of the upper continental crust (1.5 ng/g) [59] and 78.6% of the samples from the F₁₄ fault were mineralized (Figure 5a). The gentle F₇ fault between the Wujiaping and Xuman formations shows high Sb, Tl, Hg, W, Mo, and Cd contents (orange to deep red), although the F₇ fault was barren and only displayed a weak enrichment of Au (yellow; Figure 4a). Tan et al. [52] noted significant enrichment of Sb and Tl along a regional ore-conducting structure (referred to as SBT) along an unconformity between the Middle and Upper Permian at the Shuiyindong Au deposit, the largest Carlin-type deposit in the Youjiang Basin. It is plausible that the F₇ fault at Lintan bears similarities to the SBT at Shuiyindong, potentially serving as a structural conduit for transporting ore-forming fluids to the F₁₄ fault. In addition, recent isotopic studies on Mg [60], Hg [61], and noble gases (He, Ne, and Ar) [62] have shown that the ore-forming fluids of Carlin-type Au deposits in the Youjiang Basin have a magmatic origin. W, Mo, and Cd are usually enriched or mineralized and are accompanied by magma-associated hydrothermal activities [63–65]. The strong enrichment of W (Figure 5g), Mo (Figure 5i), and Cd (Figure 5l) in and around the F₇ fault suggests that these elements, along with As, Sb, Hg, and Tl, likely acted as influx elements during Au mineralization. Consequently, while the F₁₄ fault is identified as the primary ore-bearing fracture zone, the F₇ fault appears to serve as the regional ore-conducting structure of the Lintan deposit. Accordingly, the intersection site of the F₁₄ and F₇ faults emerges as an unquestionably favorable prospecting target for the Lintan Au deposit. Outside the Lintan Au deposit, faults between the Wujiaping and Xuman formations and related reverse faults are potential prospective regions. The recognition of the F₇ fault as a potential ore-conducting structure highlights the importance of understanding regional structural controls on Carlin-type gold mineralization. Future exploration efforts should focus on identifying similar regional faults and unconformities that may have acted as conduits for ore-forming fluids.

5.3. Prospecting Indicators

Anomalies of single Au and ore-related elements (i.e., As, Hg, Sb, and Tl), which usually correspond to the main Au mineralization space, are generally used to delineate the drilling targets of Carlin-type Au deposits in the Youjiang Basin [9–11]. However, this method likely neglects hidden orebodies in covered areas that commonly exhibit weak anomalies of metallogenic elements. Factor analysis is a useful tool for extracting the most information from a geochemistry dataset and reducing it to fewer independent factors [48]. The spatial distribution of a factor can reveal a consistent trend of high-loading elements, aiding in the tracking and reinforcement of mineralization trails or other geological processes [23,28]. In the Lintan deposit, F2 (As, Au, Sb, and Hg), F3 (Pb, Ag, and Mo), and F4 (Cd and Mo) extracted through factor analysis have all been demonstrated to be influenced by Au mineralization, despite each exhibiting distinct spatial distribution patterns (Figures 8 and 9). In addition, W and Tl had weak positive correlations with ore-related elements (Table 2) and displayed high contents in the F₁₄ and F₇ faults (Figure 4f,g). Therefore, Pb, Ag, Cd, Mo, and W are significant prospecting indicator elements besides Au, As, Sb, Hg, and Tl in the Lintan deposit. These findings have significant implications for future exploration efforts in the Youjiang Basin and other regions with Carlin-type gold deposits. The identification of Pb, Ag, Cd, Mo, and W as potential prospecting indicators, in addition to the conventional Au, As, Sb, Hg, and Tl, encourages explorationists to look beyond the traditional suite of pathfinder elements. This expanded toolbox of indicators can be particularly valuable in areas with concealed mineralization or weak geochemical anomalies of the typical Carlin-type pathfinder elements in the Youjiang Basin.

Factor analysis is productive for extracting the common spatial trends of elements. However, it comes with the drawback of losing a small portion of geochemical information and overlooking the differences in local spatial distributions among elements. Analyzing

the spatial relationships of each element individually in exploration geochemistry data is a time-intensive process, making it challenging to extract precise spatial relationships among elements. The association rule algorithm can uncover local spatial relationships between elements and establish quantitative indicators for exploration [21,22,30–34]. Strong association rules with high support, confidence, and lift are typically selected as prospecting indicators [27,48]. In the case of the Lintan Au deposit, Au was designated as the target element, while the remaining 14 elements were used as input for association rule analysis. This process identified 12 effective strong association rules (Table 6). These association rules can recognize Au mineralization not only through metallogenic elements (As, Sb, and Hg) but also by other trace elements (Ag, Cd, W, Mo, Ni, Tl, Cu, Co, Zn, Bi, and Pb). Rules 1–4 can be used to evaluate no mineralization, rules 5–8 to evaluate weak mineralization, and rules 9–12 to evaluate strong mineralization. These rules are consistent with the accumulated experience of predecessors, proving that they align with reality. The combination of factor analysis and association rule algorithm can take full advantage of exploration geochemistry data, which is significant for uncovering common trends among elements and finding hidden element combinations and potential correlations among elements. This demonstrates the power of combining factor analysis and association rule algorithms to extract comprehensive information from geochemical data, which can be applied to other Carlin-type gold deposits and, more broadly, to various types of mineral deposits worldwide.

6. Conclusions

(1) The 15 elements present in the rock samples from the Lintan Au deposit were categorized into four distinct groups through R-type cluster and factor analysis. Group 1 consisted of Co, Cu, Zn, Ni, Tl, W, and Bi, which were controlled by sedimentary diagenesis. Group 2 comprised Au, As, Hg, and Sb, indicating Au mineralization. Group 3 encompassed Pb, Ag, and Mo, primarily influenced by ore-forming hydrothermal activities. Lastly, Group 4 included Cd and Mo, which may have been constrained by ore-forming hydrothermal activities.

(2) The spatial distributions of the 15 elements in the Lintan Au deposit indicated that the F₁₄ fault serve as the primary ore-bearing fracture zone, while the F₇ fault acts as the ore-conducting structure. Faults situated between the Wujiaping and Xuman formations, along with associated reverse faults, represent potential prospecting targets both within and outside the Lintan Au deposit in the Youjiang Basin.

(3) Pb, Ag, Cd, Mo, and W emerged as significant prospecting indicator elements, alongside to Au, As, Sb, Hg, and Tl, in the Lintan and other Au deposits within the Youjiang Basin. Additionally, the association rule algorithm yielded 12 effective association rules, which can aid in identifying whether samples have suffered mineralization.

(4) The integration of factor analysis and association rule algorithms proves to be a prospecting method that deserves wider adoption. This approach facilitates the extraction of common trends among elements, aiding in tracking and reinforcing mineralization trails or other geological processes. Additionally, it unveils local spatial relationships between elements and establishes quantitative indicators for exploration purposes.

Supplementary Materials: The following supporting information can be downloaded at: <https://www.mdpi.com/article/10.3390/min14050492/s1>.

Author Contributions: Investigation, Z.X., K.Z., J.X. and T.R.; writing—original draft preparation, X.W. and S.C.; writing—review and editing, Q.T.; project administration, L.Z. and Y.X.; funding acquisition, J.L. and Q.T. All authors have read and agreed to the published version of the manuscript.

Funding: This research was funded by the grants from the National Key Research and Development Program of China (2023YFC2906804), Science and Technology Foundation of Guizhou Province (Qiankehezhicheng [2021] YiBan 403; Qiankehepingtairercai-CXTD [2021]007), and National Natural Science Foundation of China (42273072; 42073044).

Data Availability Statement: Data available on request due to restrictions.

Acknowledgments: We are grateful to Guizhou Jinfeng Mining Co., Ltd. for granting access to the Lintan Mine. We thank An Wang for the chemical analysis and Xingchun Zhang, Zhengle Chen, Bailin Chen, Yuke Shen, and Wengao Zhang for field guidance and fruitful discussions. We thank the anonymous reviewers for their constructive comments.

Conflicts of Interest: Lujing Zheng is an employee of Guizhou Jinfeng Mining Limited. The paper reflects the views of the scientists and not the company.

References

1. Cline, J.S.; Hofstra, A.H.; Muntean, J.L.; Tosdal, R.M.; Hickey, K.A. Carlin-type gold deposits in Nevada: Critical geologic characteristics and viable models. In *Economic Geology 100th Anniversary Volume*; Hedenquist, J.W., Thompson, J.F.H., Goldfarb, R.J., Richards, J.P., Eds.; Society of Economic Geologists, Inc.: Littleton, CO, USA, 2005; pp. 451–484.
2. Hofstra, A.H.; John, D.A.; Theodore, T.G. A special issue devoted to gold deposits in northern Nevada: Part 2. Carlin-type deposits. *Econ. Geo.* **2003**, *98*, 1063–1067. [\[CrossRef\]](#)
3. Liu, J.; Wang, Z.; Yang, C.; Li, J.; Zheng, L.; Chen, F.E.; Tan, Q.; Xie, Z.; Song, W.; Xu, L.; et al. Discriminant index and significance of structural alteration body of Carlin-type gold deposits in Yunnan-Guizhou-Guangxi and its surrounding areas, China. *Gold Sci. Technol.* **2022**, *30*, 532–539, (In Chinese with English abstract).
4. Hu, R.; Fu, S.; Huang, Y.; Zhou, M.; Fu, S.; Zhao, C.; Wang, Y.; Bi, X.; Xiao, J. The giant South China Mesozoic low-temperature metallogenic domain: Reviews and a new geodynamic model. *J. Asian Earth Sci.* **2017**, *137*, 9–34. [\[CrossRef\]](#)
5. Su, W.; Dong, W.; Zhang, X.; Shen, N.; Hu, R.; Hofstra, A.H.; Cheng, L.; Xia, Y.; Yang, K. Carlin-type gold deposits in the Dian-Qian-Gui “golden triangle” of Southwest China. In *Diversity of Carlin-Style Gold Deposits, Reviews in Economic Geology*; Muntean, J.L., Ed.; Society of Economic Geologists, Inc.: Littleton, CO, USA, 2018; Volume 20, pp. 157–185.
6. Zeng, G.; Hu, X.; Luo, D.; Liu, J.; Yao, S.; Jin, Y. Structural Control of the Getang Carlin-Type Gold Deposit in Southwest China. *J. Earth Sci.* **2024**, *35*, 536–552. [\[CrossRef\]](#)
7. Jin, X.; Yang, C.; Liu, J.; Yang, W. Source and Evolution of the Ore-Forming Fluids of Carlin-Type Gold Deposit in the Youjiang Basin, South China: Evidences from Solute Data of Fluid Inclusion Extracts. *J. Earth Sci.* **2021**, *32*, 185–194. [\[CrossRef\]](#)
8. Feng, J.Z. *Geochemical atlas of Guizhou Province*; Geological Publishing House: Beijing, China, 2008. (In Chinese)
9. Tan, Q.; Xia, Y.; Xie, Z.; Wang, Z.; Li, S.; Wei, D.; Yan, J.; Zhao, Y. Tectono-geochemistry and concealed ores prospecting in the Shuiyindong gold deposit of southwestern Guizhou. *Acta Geosci. Sin.* **2020**, *41*, 886–898, (In Chinese with English abstract).
10. Song, W.; Liu, J.; Wu, P.; Li, J.; Wang, Z.; Yang, C.; Tan, Q.; Wang, D. A successful application of the tectono-geochemistry weak information extraction method in the prospecting of Carlin-type gold deposits in southwestern Guizhou Province. *Geophys. Geochem. Explor.* **2022**, *46*, 1338–1348, (In Chinese with English abstract).
11. Li, S.; Liu, J.; Xia, Y.; Xie, Z.; Tan, Q.; Wang, Z.; Zhou, G.; Yang, C.; Meng, M.; Tan, L.; et al. Tectono-geochemistry weak mineralization information extraction method and its application in the Carlin-type gold accumulation area of southwestern Guizhou. *Gold Science and Technology* **2021**, *29*, 53–63, (In Chinese with English abstract).
12. Tan, Q.; Xia, Y.; Wang, X.; Xie, Z.; Wei, D. Carbon-oxygen isotopes and rare earth elements as an exploration vector for Carlin-type gold deposits: A case study of the Shuiyindong gold deposit, Guizhou Province, SW China. *J. Asian Earth Sci.* **2017**, *148*, 1–12. [\[CrossRef\]](#)
13. Zhang, W.; Zeng, Z.; Zhou, J.; Ji, G.; Xu, X.; Liu, G.; Lu, J. Broadband magnetotelluric(BMT)detecting blind gold deposits with interfacetype: A case of deep prospecting in the Getang area, southwestern Guizhou. *Geol. China* **2023**, *50*, 359–375, (In Chinese with English abstract).
14. Zhang, W.; Ji, G.; Liao, G.; Zhang, Q.; Gao, H.; Xiong, W.; Xia, S.; Yang, J.; Li, H. Prospecting model and exploration evaluation method offault controlled gold deposits in southwest Guizhou:a case study of Yata gold deposit. *Acta Geol. Sin.* **2021**, *95*, 3961–3978, (In Chinese with English abstract).
15. Yang, B.; Jiajun, W.; Yunnan, H.; Jianzhong, L.; Liansu, Q.; Wang, Z.; Hu, T. Electrical structural features of strata bound Carlin-type gold deposit in southwest Guizhou: Audio magnetotelluric sounding of Shuiyindong section. *Guizhou Geol.* **2016**, *33*, 1–8, (In Chinese with English abstract).
16. Ye, T.; Lv, Z.; Pang, Z.; Zhang, D.; Liu, S.; Wang, Q.; Liu, J.; Cheng, Z.; Li, C.; Xiao, K.; et al. *Theory and Method of Prospecting Prediction in Exploration Area*; Geological Publishing House: Beijing, China, 2014. (In Chinese)
17. Zhao, P.; Chi, S.; Li, Z.; Cao, X.; Wei, J. *Theories and Methods for Mineral Exploration*; China University of Geosciences Press: Wuhan, China, 2006. (In Chinese)
18. Zuo, R.; Xiong, Y. Geodata science and geochemical mapping. *J. Geochem. Explor.* **2020**, *209*, 106431. [\[CrossRef\]](#)
19. Reichstein, M.; Camps-Valls, G.; Stevens, B.; Jung, M.; Denzler, J.; Carvalhais, N.; Prabhat, F. Deep learning and process understanding for data-driven Earth system science. *Nature* **2019**, *566*, 195–204. [\[CrossRef\]](#)
20. Zuo, R. Machine learning of mineralization-related geochemical anomalies: A review of potential methods. *Nat. Resour. Res.* **2017**, *26*, 457–464. [\[CrossRef\]](#)
21. Mao, X.; Tang, M.; Deng, H.; Chen, J.; Liu, Z.; Wang, J. Using association rules analysis to determine favorable mineralization sites in the Jiaojia gold belt, Jiaodong Peninsula, East China. *Front. Earth Sci.* **2023**, *11*, 1174017. [\[CrossRef\]](#)

22. Chen, M.; Luo, X.; Zhu, Y.; Li, Y.; Zhao, W.; Wu, J. An apriori-based learning scheme towards intelligent mining of association rules for geological big data. *Intell. Autom. Soft Co.* **2020**, *26*, 973–987. [\[CrossRef\]](#)
23. Ouchchen, M.; Boutaleb, S.; Abia, E.H.; El Azzab, D.; Miftah, A.; Dadi, B.; Echogdali, F.Z.; Mamouch, Y.; Pradhan, B.; Santosh, M.; et al. Exploration targeting of copper deposits using staged factor analysis, geochemical mineralization prospectivity index, and fractal model (Western Anti-Atlas, Morocco). *Ore Geol. Rev.* **2022**, *143*, 104762. [\[CrossRef\]](#)
24. Afzal, P.; Mirzaei, M.; Yousefi, M.; Adib, A.; Khalajmasoumi, M.; Zarifi, A.Z.; Foster, P.; Yasrebi, A.B. Delineation of geochemical anomalies based on stream sediment data utilizing fractal modeling and staged factor analysis. *J. Afr. Earth Sci.* **2016**, *119*, 139–149. [\[CrossRef\]](#)
25. Yousefi, M.; Kamkar-Rouhani, A.; Carranza, E.J.M. Application of staged factor analysis and logistic function to create a fuzzy stream sediment geochemical evidence layer for mineral prospectivity mapping. *Geochem. Explor. Env. A.* **2014**, *14*, 45–58. [\[CrossRef\]](#)
26. Reimann, C.; Filzmoser, P.; Garrett, R.G. Factor analysis applied to regional geochemical data: Problems and possibilities. *Appl. Geochem.* **2002**, *17*, 185–206. [\[CrossRef\]](#)
27. Liu, X.; Zhou, Y. Application of association rule algorithm in studying abnormal elemental associations in the Pangxidong area in western Guangdong Province, China. *Earth Sci. Front.* **2019**, *26*, 125–130, (In Chinese with English abstract).
28. Tripathi, V.S. Factor analysis in geochemical exploration. *J. Geochem. Explor.* **1979**, *11*, 263–275. [\[CrossRef\]](#)
29. Sadeghi, M.; Billay, A.; Carranza, E.J.M. Analysis and mapping of soil geochemical anomalies: Implications for bedrock mapping and gold exploration in Giyani area, South Africa. *J. Geochem. Explor.* **2015**, *154*, 180–193. [\[CrossRef\]](#)
30. Agrawal, R.; Imielinski, T.; Swami, A. Mining association rules between sets of items in large databases. In Proceedings of the 1993 ACM SIGMOD Conference, Washington, DC, USA, 26–28 May 1993; pp. 1–10.
31. Chang, L.; Zhu, Y.; Zhang, G.; Zhang, X.; Hu, B. Spatial correlation analysis of mineral resources information. *Acta Petrol. Sin.* **2018**, *34*, 314–318, (In Chinese with English abstract).
32. Han, D.; Shi, Y.; Wang, W.; Dai, Y. Research on multi-level association rules based on geosciences data. *J. Softw.* **2013**, *8*, 3269–3276. [\[CrossRef\]](#)
33. Ding, W.; Eick, C.F.; Yuan, X.; Wang, J.; Nicot, J.-P. A framework for regional association rule mining and scoping in spatial datasets. *Geoinformatica* **2011**, *15*, 1–28. [\[CrossRef\]](#)
34. Kotsiantis, S.; Kanellopoulos, D. Association rules mining: A recent overview. *GESTS Int. Trans. Comput. Sci. Eng.* **2005**, *32*, 71–82.
35. Du, Y.; Huang, H.; Yang, J.; Huang, H.; Tao, P.; Huang, Z.; Hu, L.; Xie, C. The basin translation from late Paleozoic to Triassic of the Youjiang basin and its tectonic signification. *Geol. Rev.* **2013**, *59*, 1–11, (In Chinese with English abstract).
36. Du, Y.; Huang, H.; Huang, Z.; Xu, Y.; Yang, J.; Huang, H. Basin translation from Late Palaeozoic to Triassic of Youjiang Basin and its tectonic significance. *Geol. Sci. Technol. Inf.* **2009**, *28*, 10–15, (In Chinese with English abstract).
37. Hu, R.; Su, W.; Bi, X.; Tu, G.; Hofstra, A.H. Geology and geochemistry of Carlin-type gold deposits in China. *Miner. Deposita* **2002**, *37*, 378–392.
38. Zaw, K.; Meffre, S.; Lai, C.K.; Burrett, C.; Santosh, M.; Graham, I.; Manaka, T.; Salam, A.; Kamvong, T.; Cromie, P. Tectonics and metallogeny of mainland Southeast Asia—A review and contribution. *Gondwana Res.* **2014**, *26*, 5–30.
39. Lai, C.K.; Meffre, S.; Crawford, A.J.; Zaw, K.; Xue, C.D.; Halpin, J.A. The Western Ailaoshan Volcanic Belts and their SE Asia connection: A new tectonic model for the Eastern Indochina Block. *Gondwana Res.* **2014**, *26*, 52–74. [\[CrossRef\]](#)
40. Li, Z.; Li, X. Formation of the 1300-km-wide intracontinental orogen and postorogenic magmatic province in Mesozoic South China: A flat-slab subduction model. *Geology* **2007**, *35*, 179–182. [\[CrossRef\]](#)
41. Zheng, L.; Tan, Q.; Zuo, Y.; Xia, Y.; Xie, Z.; Zheng, L.; Liu, J. Two hydrothermal events associated with Au mineralization in the Youjiang Basin, southwestern China. *Ore Geol. Rev.* **2022**, *144*, 104816. [\[CrossRef\]](#)
42. Tan, Q.; Xia, Y.; Xie, Z.; Wang, Z.; Wei, D.; Zhao, Y.; Yan, J.; Li, S. Two hydrothermal events at the Shuiyindong Carlin-Type gold deposit in Southwestern China: Insight from Sm–Nd dating of fluorite and calcite. *Minerals* **2019**, *9*, 230. [\[CrossRef\]](#)
43. Zhou, M.; Zhao, J.; Qi, L.; Su, W.; Hu, R. Zircon U–Pb geochronology and elemental and Sr–Nd isotope geochemistry of Permian mafic rocks in the Funing area, SW China. *Contrib. Mineral. Petr.* **2006**, *151*, 1–19. [\[CrossRef\]](#)
44. Fan, W.M.; Zhang, C.H.; Wang, Y.J.; Guo, F.; Peng, T.P. Geochronology and geochemistry of Permian basalts in western Guangxi Province, Southwest China: Evidence for plume-litho sphere interaction. *Lithos* **2008**, *102*, 218–236. [\[CrossRef\]](#)
45. Liu, S.; Su, W.; Hu, R.; Feng, C.; Gao, S.; Coulson, I.M.; Wang, T.; Feng, G.; Tao, Y.; Xia, Y. Geochronological and geochemical constraints on the petrogenesis of alkaline ultramafic dykes from southwest Guizhou Province, SW China. *Lithos* **2010**, *114*, 253–264. [\[CrossRef\]](#)
46. Chen, M.; Zhang, Y.; Meng, Y.; Lu, G.; Liu, S. Determination of upper limit of metallogenic epoch of Liaotun gold deposit in western Guangxi and its implications for chronology of Carlin-type gold deposits in Yunnan-Guizhou-Guangxi golden triangle area. *Miner. Depos.* **2014**, *33*, 1–13, (In Chinese with English abstract).
47. Su, W.; Zhang, H.; Hu, R.; Ge, X.; Xia, B.; Chen, Y.; Zhu, C. Mineralogy and geochemistry of gold-bearing arsenian pyrite from the Shuiyindong Carlin-type gold deposit, Guizhou, China: Implications for gold depositional processes. *Miner. Depos.* **2012**, *47*, 653–662. [\[CrossRef\]](#)
48. Zhou, Y.; Zhang, L.; Zhang, A.; Wang, J. *Earth Science Big Data Mining and Machine Learning*; Sun Yat-sen University Press: Guangzhou, China, 2018. (In Chinese)
49. Härdle, W.; Simar, L. *Applied Multivariate Statistical Analysis*, 2nd ed.; Springer: Berlin/Heidelberg, Germany, 2007.

50. Seyedrahipi-Niaraq, M.; Mahdiyanfar, H. Introducing a new approach of geochemical anomaly intensity index (GAIL) for increasing the probability of exploration of shear zone gold mineralization. *Geochemistry* **2021**, *81*, 125830. [[CrossRef](#)]
51. Cheng, Q. Mapping singularities with stream sediment geochemical data for prediction of undiscovered mineral deposits in Gejiu, Yunnan Province, China. *Ore Geol. Rev.* **2007**, *32*, 314–324. [[CrossRef](#)]
52. Tan, Q.; Xia, Y.; Xie, Z.; Yan, J. Migration paths and precipitation mechanisms of ore-forming fluids at the Shuiyindong Carlin-type gold deposit, Guizhou, China. *Ore Geol. Rev.* **2015**, *69*, 140–156. [[CrossRef](#)]
53. Hu, R.; Gao, W.; Fu, S.; Su, W.; Peng, J.; Bi, X. Mesozoic intraplate metallogenesis in South China. *Earth Sci. Front.* **2024**, *in press*. (In Chinese with English abstract).
54. Liu, J.; Wang, Z.; Song, W.; Wang, D.; Yang, C.; Li, J.; Zheng, L.; Li, S.; Tan, Q.; Xie, Z.; et al. Construction and prospecting practice of multilevel structural detachment metallogenic system of Carlin-type gold deposits in Yunnan-Guizhou-Guangxi area. *Geol. Rev.* **2023**, *69*, 513–525. (In Chinese with English abstract).
55. Xie, X. Exploration geochemistry: Present status and prospects. *Geol. Rev.* **1996**, *42*, 346–356. (In Chinese with English abstract).
56. Hickey, K.A.; Ahmed, A.D.; Barker, S.L.; Leonardson, R. Fault-controlled lateral fluid flow underneath and into a Carlin-type gold deposit: Isotopic and geochemical footprints. *Econ. Geo.* **2014**, *109*, 1431–1460. [[CrossRef](#)]
57. Vaughan, J.R.; Hickey, K.; Barker, S.; Dipple, G.M. Stable isotopes and fluid flow pathways in the Banshee Carlin-type gold deposit. In *Smart Science for Exploration and Mining, Vol 1 and 2*; Williams, P.J., Ed.; James Cook University: Townsville, QLD, Australia, 2010; pp. 266–268.
58. Muntean, J.L.; Cassinero, M.D.; Arehart, G.B.; Cline, J.S.; Longo, A.A. Fluid pathways at the Turquoise Ridge Carlin-type gold deposit, Getchell district, Nevada. In *Smart Science for Exploration and Mining, Vol 1 and 2*; Williams, P.J., Ed.; James Cook University: Townsville, QLD, Australia, 2010; pp. 251–253.
59. Rudnick, R.L.; Gao, S. Composition of the continental crust. In *Treatise on Geochemistry*; Holland, H.D., Turekian, K.K., Eds.; Elsevier: Oxford, UK, 2014; Volume 3, pp. 1–64.
60. Xie, Z.; Huang, K.-J.; Xia, Y.; Cline, J.; Tan, Q.; Liu, J.; Xiao, J.; Yan, B. Heavy $\delta^{26}\text{Mg}$ values in carbonate indicate a magmatic-hydrothermal origin of Carlin-type Au deposit. *Geochim. Cosmochim. Acta* **2022**, *333*, 166–183. [[CrossRef](#)]
61. Gao, W.; Hu, R.; Wang, X.; Yin, R.; Bi, X.; Xie, Z.; Fu, S.; Yan, J. Large-scale basement mobilization endows the giant Carlin-type gold mineralization in the Youjiang Basin, South China: Insights from mercury isotopes. *GSA Bulletin* **2023**, *135*, 3163–3172. [[CrossRef](#)]
62. Jin, X.; Hofstra, A.H.; Hunt, A.G.; Liu, J.; Yang, W.; Li, J. Noble gases fingerprint the source and evolution of ore-forming fluids of Carlin-type gold deposits in the golden triangle, south China. *Econ. Geo.* **2020**, *115*, 455–469. [[CrossRef](#)]
63. Hou, Z.; Duan, L.; Lu, Y.; Zheng, Y.; Zhu, D.; Yang, Z.; Yang, Z.; Wang, B.; Pei, Y.; Zhao, Z.; et al. Lithospheric architecture of the Lhasa Terrane and its control on ore deposits in the Himalayan-Tibetan Orogen. *Econ. Geo.* **2015**, *110*, 1541–1575. [[CrossRef](#)]
64. Deng, J.; Wang, Q.; Li, G.; Li, C.; Wang, C. Tethys tectonic evolution and its bearing on the distribution of important mineral deposits in the Sanjiang region, SW China. *Gondwana Res.* **2014**, *26*, 419–437. [[CrossRef](#)]
65. Mao, J.; Cheng, Y.; Chen, M.; Pirajno, F. Major types and time-space distribution of Mesozoic ore deposits in South China and their geodynamic settings. *Miner. Deposita* **2013**, *48*, 267–294.

Disclaimer/Publisher’s Note: The statements, opinions and data contained in all publications are solely those of the individual author(s) and contributor(s) and not of MDPI and/or the editor(s). MDPI and/or the editor(s) disclaim responsibility for any injury to people or property resulting from any ideas, methods, instructions or products referred to in the content.